Corrosion Science 178 (2021) 109095

Contents lists available at ScienceDirect

Corrosion Science

journal homepage: www.elsevier.com/locate/corsci

Multiphysics modeling and uncertainty quantification of tribocorrosion in aluminum alloys

Kaiwen Wang [a], Yinan Wang [b], Xiaowei Yue [b,*], Wenjun Cai [a,*]

[a] Department of Materials Science and Engineering, Virginia Polytechnic Institute and State University, Blacksburg, VA 24060, USA
[b] Department of Industrial and Systems Engineering, Virginia Polytechnic Institute and State University, Blacksburg, VA 24060, USA

ARTICLE INFO

Keywords:
Al alloys
Tribocorrosion
Finite element analysis
Uncertainty quantification

ABSTRACT

Past research in tribocorrosion mainly relies on costly and trial-and-error experimental methods to study the materials' deformation and degradation under extreme conditions. This work developed a finite element based multiphysics model, validated by existing tribocorrosion experiments of two Al alloys, to analyze the synergistic effects of mechanical and corrosion properties on the material degradation mechanisms of tribocorrosion. During consecutive passes of the counter body, significant residual stress was found to develop near the edge of the wear track, leading to highly concentrated corrosion current than elsewhere. Such non-uniform surface corrosion and stress-corrosion coupling led to variations of tribocorrosion rate over time, even though testing conditions were kept constant. Tribocorrosion rate maps were generated to predict material loss as a function of different mechanical and electrochemical properties, indicating a hard, complaint metal with high anodic Tafel slope and low exchange current density is most resistant to tribocorrosion. Finally, two surrogate models, Gaussian process and neural network with dropout, were used for uncertainty quantification of the finite element model.

1. Introduction

The design of robust and reliable metals and alloys that are simultaneously wear and corrosion resistant is crucial for various applications such as oil and gas pipelines, underwater vehicles, batteries, and biomedical devices where high mechanical stress and corrosive environment coexist [1–6]. During tribocorrosion, the coupling of stress (either external or residual) and corrosion is a major potential threat to jeopardize materials' long-term sustainability and structural integrity. The stresses at the contacting asperities not only plastically deform the surface material, leading to the formation of wear debris, tribolayer, and mechanically deformed layer, but also enhance localized corrosion on the wear track [7–9]. Such wear-corrosion synergy is especially significant for passive metals such as aluminum (Al) alloys, which relies on the presence of an ultrathin (~ a few nm) surface oxide layer (i.e., passive layer) for corrosion protection under passivating conditions (e.g., neutral aqueous solution for Al) [8,10]. When this delicate passive layer is mechanically removed, the wear-corrosion synergy has often been found to enhance the corrosion process and accelerate total material loss [1,11–14], although the opposite has also been reported [15,16]. For example, Jemmely et al. [11] reported an experimental investigation on the tribocorrosion behavior of Fe–17Cr stainless steel under reciprocal wear using alumina pin as a counter body in acid and alkaline solutions. They found that the interdependence of the mechanical and the electrochemical response is affected by the solution pH, in which the metal exhibited different repassivation behavior. Vieira et al. [14] studied the tribocorrosion resistance of Al alloys in NaCl and $NaNO_3$ solutions and proposed a theory attributing the enhanced localized corrosion to the galvanic coupling between the passive area and depassivated wear track during tribocorrosion. While many studies reported a positive wear-corrosion synergy, the opposite has also been reported. For example, Bello et al. [15] observed a negative synergy in S31603 and S32760 stainless steels under a low abrasion rate. It was argued that under such conditions, the tribocorrosion material loss is smaller than that of pure wear condition due to the simultaneous mechanical and electrochemical attack, where corrosion-induced passive film on the surface reduced the overall two-body abrasion.

So far, most works focus on experimental study and phenomenological modeling of tribocorrosion [12], only limited work has been done to develop a numerical simulation framework that couples materials' mechanical and electrochemical responses as well as their synergy. Despite limited research, several studies have been carried out to

* Corresponding authors.
E-mail addresses: xyw@vt.edu (X. Yue), caiw@vt.edu (W. Cai).

https://doi.org/10.1016/j.corsci.2020.109095
Received 11 July 2020; Received in revised form 14 October 2020; Accepted 29 October 2020
Available online 2 November 2020
0010-938X/

investigate wear [17–20], corrosion [21–24], and stressed corrosion [25–27] of metals and alloys using finite element analysis (FEA) based methods. For example, Xu et al. published a series of works [25,26] investigating the corrosion of steel in pipelines under tensile stress using FEA methods. Wang et al. created a model using a combination of cellular automata and FEA methods for metastable pitting corrosion under mechanical stress [27]. However, such models cannot be directly applied to tribocorrosion, where the material degradation and deformation is multi-physics in nature, requiring consideration of the time-dependent surface evolution and material loss caused by elastic/-plastic deformation, corrosion, and stress-corrosion synergy on the wear track. This work aims to develop an experimentally validated computational framework to model and predict tribocorrosion behavior of metals, using Al alloys as examples. It is believed that the developed model, material property extraction, validation, and uncertainty quantification processes can be extended to metal systems beyond Al alloys in future studies.

Due to its lightweight, high specific strength, and good corrosion resistance, Al alloys have been heavily used in seawater such as offshore infrastructures, ships, and undersea vehicles, whose structural integrity and useful lifetime rely heavily on the tribocorrosion properties of the alloy [28,29]. The pure corrosion mechanisms of Al in seawater (often approximated as neutral 0.6 M NaCl solution) has been subjected to extensive prior study [8,30]. Despite diverse corrosion kinetics that is heavily dependent on their composition and microstructure, the thermodynamics of Al alloy corrosion is well understood. The anodic reaction is mainly aluminum oxidation, expressed as $Al = Al^{3+} + 3e^-$, which has a standard equilibrium potential of -1.662 V (vs. SHE) [31]. The cathodic reaction is governed by oxygen reduction in neutral solution via $O_2 + 2H_2O + 4e^- = 4OH^-$, with a standard equilibrium potential of 0.82 V [31]. According to Nernst equation, the equilibrium potential of aluminum oxidation is affected by the concentration of aluminum ions following the equation:

$$E_{\frac{Al}{Al^{3+}}} = -1.66 + \frac{0.059}{3}\log\left(Al^{3+}\right) \tag{1}$$

and the equilibrium potential of oxygen reduction is affected by the pH of the solution following

$$E_{\frac{H^+}{H_2}} = 0.82 - 0.059pH \tag{2}$$

The corrosion kinetics of Al and its alloys is often measured experimentally using polarization methods. For example, Fig. 1 demonstrates the potentiodynamic polarization curve of pure Al in neutral 0.6 M NaCl. Assuming the electrochemical reaction takes place directly on the metal and the system has only one time constant, given the theoretical equilibrium potential (i.e. E_a and E_c for the anodic and cathodic reaction respectively), kinetic parameters such as Tafel slopes and exchange current densities (i_a and i_c) of the reactions could be obtained.

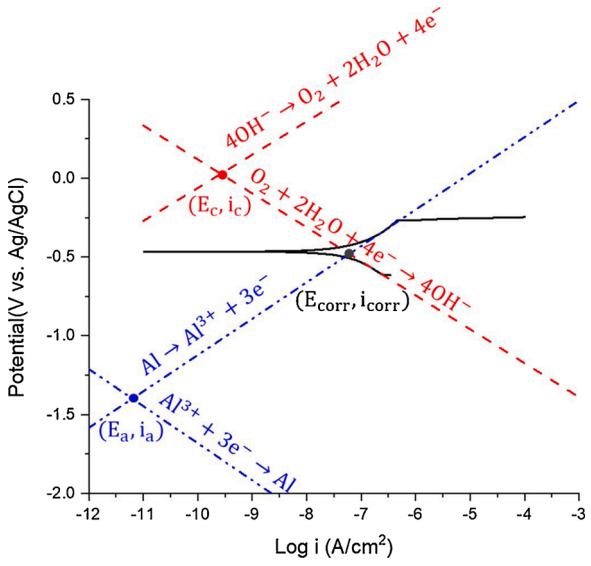

Fig. 1. Typical potentiodynamic polarization curve of Al corrosion in 0.6 M NaCl at pH = 6.4.

During tribocorrosion of Al alloys in seawater, our prior work showed that both alloy composition and testing parameters affect the overall tribocorrosion kinetics [6,28]. Briefly, two tribocorrosion resistant Al-Mn alloys were prepared by magnetron sputtering with 5.2 at% and 20.5 at% Mn (named A5 and A20 respectively hereafter). Both the mechanical strength and corrosion resistance of Al increased with Mn% content in the alloy. During the tribocorrosion test in 0.6 M NaCl solution with a pH of ~ 6.4, it was found that when the surfaces of the samples were scratched, the open circuit potential experienced a cathodic shift and the current flowing through the electrode/electrolyte interface increased, indicating a positive wear-corrosion synergy. In addition, A20 experienced less wear-corrosion synergy and higher repassivation rate than that of A5. In a follow-up study [28], it was found that the total tribocorrosion rate, including both mechanical and chemical wear, increased with increasing scratching frequency (hence depassivation rate). The percentage of depassivated area on the wear track of A20 decreased from 70 % to 63 % when the sliding frequency was increased from 0.1 Hz to 1 Hz.

The goals of this work are to (1) develop an experimentally validated finite element based multiphysics model to quantify the effects of materials' mechanical and electrochemical properties on their tribocorrosion behavior, (2) evaluate the effects of applied surface stress as well as residual subsurface stress/strain on the corrosion kinetics, (3) develop a tribocorrosion map for material loss prediction based on both mechanical (e.g., elastic modulus and yield strength) and electrochemical (e.g., Tafel slopes) properties, and (4) quantify the FEA model uncertainty using surrogate models. In the present work, the developed FEA model will be validated using A5 and A20, whose corrosion, mechanical, and tribocorrosion properties have been well characterized by our prior experimental work [6,28,32]. In addition, the difference in alloy composition between the two allows the evaluation of different mechanical and corrosion properties on the overall tribocorrosion response. This model differs from existing phenomenological models in a way that it considers not only the dynamic process of scratching, but also the time-dependent evolution of the dissolving surface during tribocorrosion. The model paves way for a numerical method of investigating materials' tribocorrosion resistance, which could be further developed to analyze the reliability of structures and devices under extreme conditions where stress and corrosion coexist. Finally, since materials' behavior during tribocorrosion is complicated and nonlinear, uncertainty quantification (UQ) was carried out to evaluate the accuracy of the FEA model. Traditionally, Monte Carlo simulation [33] is considered as a standard approach to implementing UQ in the simulation of complex nonlinear systems. This method will repeat simulations multiple times assuming different values of unknown input parameters, which makes the computational cost grow significantly when the system has a large number of unknown parameters (e.g., various mechanical and electrochemical properties in tribocorrosion). To reduce the computation cost, two data-driven surrogate models, Gaussian Process (GP) [34] and Neural Network (NN) with dropout [35], were used here to evaluate the UQ of the developed FEA simulations [36,37]. The structure of the paper is as follows. FEA model setup is presented in Section 2. Section 3 discusses the procedures for extracting material properties from experiments. Section 4 summarizes FEA model results and validation from theories and prior experiments. Section 5 discusses the uncertainty quantification study. Concluding remarks are presented in Sections 6.

2. FEA model setup

2.1. Model geometry setup and meshing

FEA models were developed using the COMSOL Multiphysics software of version 5.3. The simulation contains three parts: nanoindentation, corrosion, and tribocorrosion. The first part is required to simulate the nanoindentation behavior of the alloys to correctly extract key mechanical properties of the alloy, Young's modulus and hardness, which are then used as inputs in the tribocorrosion model. It is noted here while these properties are typically reported from experimental measurements using the Oliver-Pharr method [38], it is shown later in Section 3, that directly using such values leads to measurable discrepancies between simulated and measured load-displacement curves. The second part considers pure corrosion of the indented surface, and the third part simulates material loss due to simultaneous scratch and corrosion.

Fig. 2 shows the geometry and meshing of the simulation. A conical diamond tip with a radius of 1 μm and an alumina ball tip with a radius of 2 mm were used for the indentation and tribocorrosion test, respectively, in consistent with the experiments. 2D axisymmetric model was used to save computational time and resource for indentation simulation. As shown in Fig. 2(b), the conical indenter with a semiapical angle of 70.3° was smoothed at the tip using the fillet option [39]. For tribocorossion, a ball-on-plate configuration shown in Fig. 2(c) was used for the 3D model geometry. Both dimensions of the counter body and sample were the same as those from experiments. The 3D FE model was simulated by half in geometry due to the presence of mirror symmetry along the symmetry (x–z) plane (Fig. 2(d)). Friction coefficient for both samples is set to be 0.6, as measured from experiment. The meshing schemes are shown in Fig. 2(b) and (d), where mesh size increases from the contact areas to areas far away. Specifically, for the indentation model, triangular mesh of 0.02~0.05 μm was used in the contact area and 0.2 μm far away. For the tribocorrosion model, the mesh size was 0.1 mm in the contact area and 0.5 mm far away. All meshing sizes were chosen after convergence analysis by balancing computational time and model accuracy where further reducing the mesh size does not affect the simulation results.

2.2. Equations and boundary conditions for contact mechanics

With the meshed geometry, mechanical module within COMSOL was applied to investigate the stress and strain responds to the external force. The contact problems are solved by defining a contact pair with a source boundary, which is the boundary of the harder material typically, and a destination boundary, which is the softer material in comparison. The normal contact pressure between destination and source boundaries is matched using the augmented Lagrangian method.

The Al alloy and indenter are modeled as elastic-perfectly plastic materials with no strain hardening during plastic deformation. The correlation between stress and strain within the elastic limit of the material could be expressed as:

$$\begin{bmatrix}\sigma_x\\ \sigma_y\\ \sigma_z\\ \sigma_{xy}\\ \sigma_{yz}\\ \sigma_{xz}\end{bmatrix} = D\left(\begin{bmatrix}\varepsilon_x\\ \varepsilon_y\\ \varepsilon_z\\ \varepsilon_{xy}\\ \varepsilon_{yz}\\ \varepsilon_{xz}\end{bmatrix} - \begin{bmatrix}\varepsilon_x\\ \varepsilon_y\\ \varepsilon_z\\ \varepsilon_{xy}\\ \varepsilon_{yz}\\ \varepsilon_{xz}\end{bmatrix}_{inel}\right) \tag{3}$$

where σ and ε stands for the 3D stress and strain components, ε_{inel} stands for the inelastic part of the strain, and D is the elasticity tensor defined as a function of elastic modulus (E) and Poisson's ratio (ν) as:

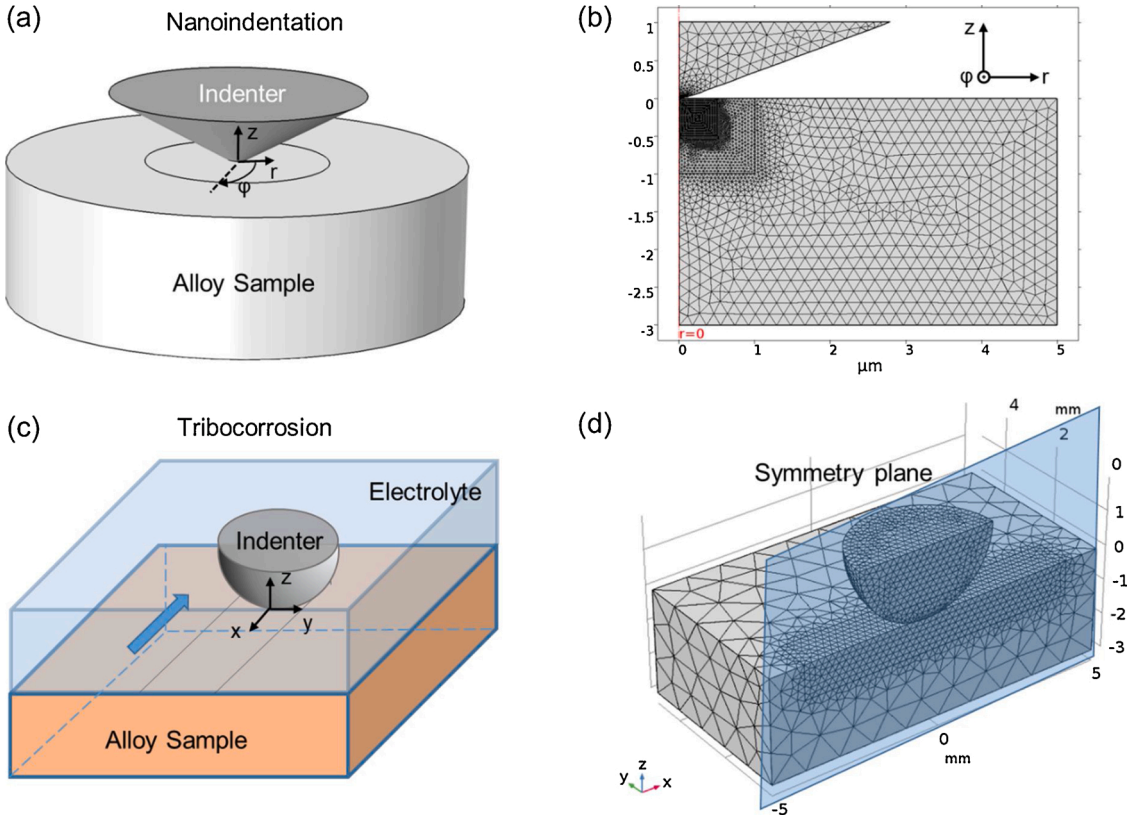

Fig. 2. (a, c) Schematic and (b, d) FEA meshing setup of the nanoindentation and tribocorrosion test model.

$$D = \frac{E}{(1+\nu)(1-2\nu)}\begin{pmatrix} 1-\nu & \nu & \nu & 0 & 0 & 0 \\ \nu & 1-\nu & \nu & 0 & 0 & 0 \\ \nu & \nu & 1-\nu & 0 & 0 & 0 \\ 0 & 0 & 0 & \frac{1-2\nu}{2} & 0 & 0 \\ 0 & 0 & 0 & 0 & \frac{1-2\nu}{2} & 0 \\ 0 & 0 & 0 & 0 & 0 & \frac{1-2\nu}{2} \end{pmatrix} \tag{4}$$

The yield surface was calculated using von Mises criterion, which could be generally expressed as

$$F = \sqrt{3J_2} - \sigma_y = 0 \tag{5}$$

In eq. (5), the first term is the von Mises stress, in which $J_2 = \frac{1}{6}\left((\sigma_x-\sigma_y)^2 + (\sigma_y-\sigma_z)^2 + (\sigma_z-\sigma_x)^2\right) + \sigma_{xy}^2 + \sigma_{yz}^2 + \sigma_{xz}^2$, and the second term is the yield strength (σ_y). The load is defined using the surface integration reaction pressure on the top surface of the indenter, imposed using auxiliary sweep method with a total of 10 steps of equal increment and decrement respectively in the range of 0 to the maximum load to simulate a quasi-dynamic process. The bottom boundary of the sample is set as a fixed constraint with no normal displacement.

2.3. Material removal by abrasive wear

After simulating the sliding contact, a strain-based material removal model was applied to simulate the wear debris generation process where contacting asperities experience highly plastic deformation and detach from the bulk. Following that proposed by Nélias et al. [40] and Bosman et al. [41], it is assumed that material removal would occur when the plastic strain ε_p exceeds a critical value ε_c. In this work, ε_c is chosen to be 0.05, which is the threshold when material experience transition from small strain deformation to severe wear [40]. The algorithm is realized by assessing the state of every element starting from that closest to the surface along the -z direction. If the obtained ε_p is larger than ε_c, the element is considered as a worn element and removed. The same process was then repeated on the element beneath it until an element with $\varepsilon_p < \varepsilon_c$ was found (unworn element). The final worn track surface profile is obtained after all surface locations are evaluated using this method.

2.4. Equations and boundary conditions for corrosion

The current density ($\boldsymbol{i}$) and the electrolyte potential (ϕ) satisfy the differential equations of:

$$\begin{cases} \nabla \cdot \boldsymbol{i_l} = Q_l \\ \boldsymbol{i_l} = -\sigma_l \nabla \phi_{elec} \end{cases} \tag{7}$$

where Q_l is the charge density in the solution, which is 0 in a solution with equal positive and negative ions. σ_l is the conductivity of the solution, which is 0.05 S/m for 0.6 NaCl aqueous solution. At the electrolyte/electrode interface, the local current density (i_{loc}) was assumed to satisfy the Tafel equation:

$$i_{loc} = 10^{\frac{\eta}{A}} i_0 \tag{8}$$

in which the overpotential (η) is defined as $\eta = \phi_{ext} - \phi_{elec} - E_{eq}$. ϕ_{ext} is the external potential connected to the metal, which is 0 V in our case. ϕ_{elec} is the electrolyte potential and E_{eq} is the corresponding equilibrium potential of the reaction happened at this interface. The boundary conditions at the interface are expressed as

$$\begin{cases} \phi_{ext} = 0 \\ n \cdot \boldsymbol{i_l} = \sum_m i_{loc,m} \end{cases} \tag{9}$$

Once the local current distribution is calculated by solving the equations above, the dissolution speed normal to the metal surface (v_n) is calculated according to Faraday's laws:

$$v_n = \frac{i_{loc} M}{nF\rho} \tag{10}$$

where M is the molar mass, n is the number of electrons transferred in dissolving 1 metal atom, F is the Faraday's constant (96,485 C/mol), and ρ is the density of the metal. The electrolyte-electrode interface was set as a free-deforming surface while the other boundaries of the sample are non-deforming ones which doesn't allow normal displacement. The elements on the free-deforming surface shrink according to the calculated dissolution speed from eqn. (10).

The depassivation and repassivation process was simulated using the thickness-dependent electrical resistor property of the surface film. The conductivity of the intact surface film (σ) was set to be $1 \times 10^{-12} S/m$, corresponding to that of Al_2O_3. The initial film thickness is set to be 4 nm, as observed in experiments [42]. During scratch induced depassivation, this thin layer is assumed to be destroyed on the wear track. In the subsequent repassivation, the film thickness grows from zero according to the dissolution rate and the electrical resistance at the surface increases. Suppose the corroded thickness of Al at a certain location and time is d, the accumulated passive layer thickness is $1.29d$, calculated from their molar volume ratio (i.e. M_{Al2O3}/M_{Al}). A resistant barrier with local conductivity per unit area of $1.29\sigma d$ is applied.

2.5. Wear-corrosion synergy and tribocorrosion

The wear-corrosion synergy during tribocorrosion was modeled by incorporating the change in electrochemical performance caused by mechanical deformation. Specifically, the anodic potential (φ_a) is assumed to shift cathodically from its equilibrium value (φ_{a0}) depending on the elastic and plastic strain following [25,43]:

$$\varphi_a = \varphi_{a0} - \frac{\sigma V_m}{nF} - \frac{TR}{nF}\ln\left(K_\alpha(\varepsilon_p)\right), \tag{11}$$

where the second and third term is the shift of equilibrium potential due to elastic and plastic deformation respectively. In Eq. (11), the stress σ is taken as the stress within the elastic deformation and for the area that is plasticly deformed, it equals to the yield strength, V_m is the molar volume of aluminum ($V_m = 9.99 \times 10^{-6} m^3/mol$), T is temperature (T = 298 K at room temperature), R is the ideal gas constant (R= 8.3145J/(mol·K)), ε_p is the effective plastic strain, and $K_\alpha(\varepsilon_p)$ is a function denoting the dislocation density increment under plastic strain (ε_p), obtained by interpolating data from [44].

The flowchart of the whole tribocorrosion model is illustrated in Fig. 3. In the simulation for tribocorrosion test, the deformed surface geometry and plastic strain after unloading obtained from wear simulation was imported as input to calculate φ_a following the Eq. (11) above at each single location on the sample surface. All the other parameters and settings are the same as the pure corrosion model.

3. Extraction of material properties from experiments

3.1. Extraction of mechanical properties

Prior nanoindentation results of A5 and A20 are used to extract Young's modulus (E) and hardness (H) of both samples. As shown in Fig. 4(a), directly using E and H values obtained experimentally from the Oliver and Pharr method (listed in Table 1) leads to a large discrepancy

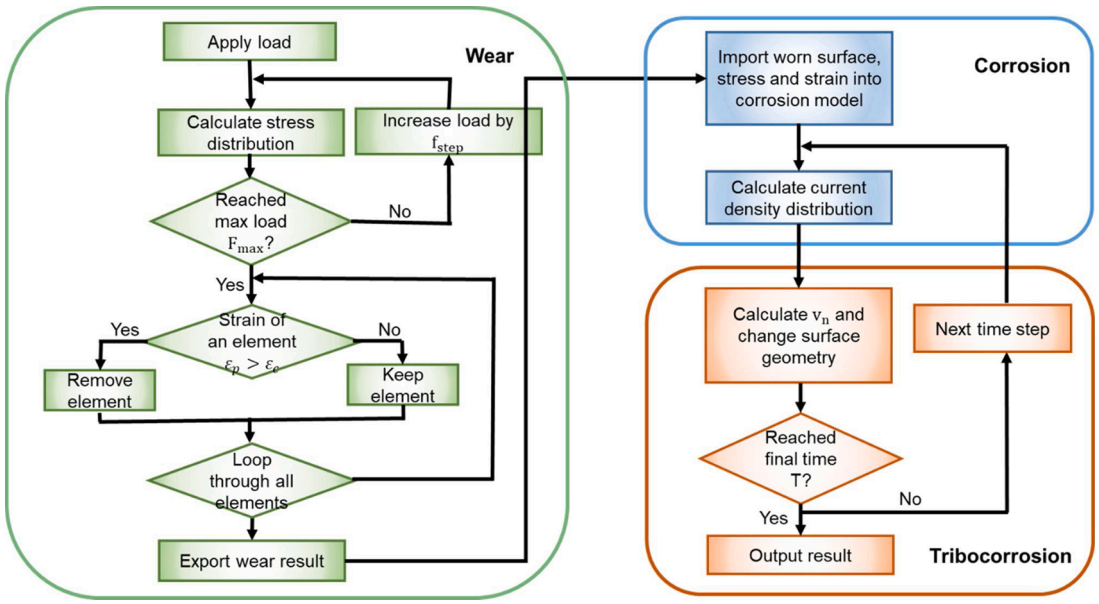

Fig. 3. Flowchart of the FEA tribocorrosion model.

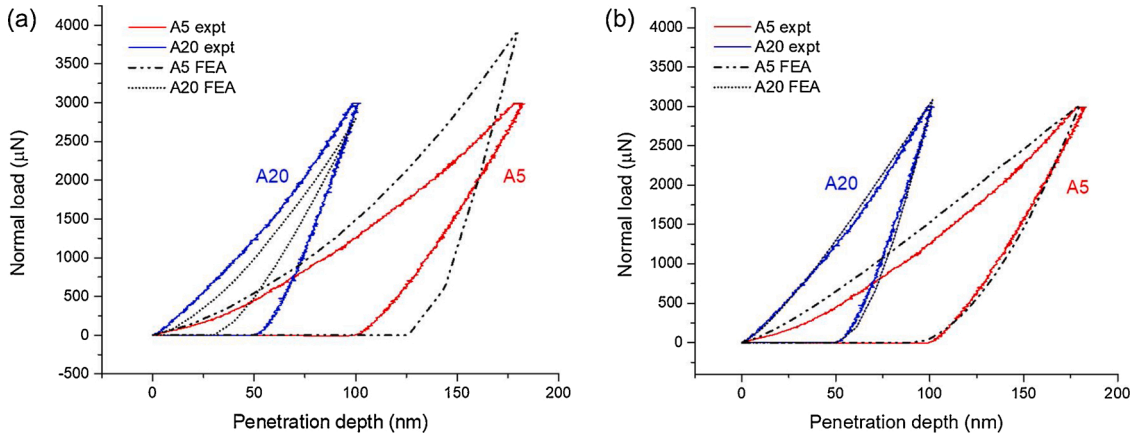

Fig. 4. Comparison of nanoindentation load-displacement curves between experiments and FEA simulations for A5 and A20 samples using (a) experimentally obtained, and (b) FEA fitted mechanical property data.

Table 1
Summary of mechanical properties from experiments and FEA simulation. E and σ_y represents elastic modulus and yield strength respectively.

Sample ID	Experiment		FEA simulation	
	E (GPa)	σ_y(GPa)	E (GPa)	σ_y(GPa)
A5	77.65	0.53	55.11	1.26
A20	97.54	1.80	108.83	2.59

between the experimental and simulated load-displacement curves. An accurate capture of such relationship is critical to model tribocorrosion, during which each location along the wear track experiences cyclic loading and unloading as the indenter passes through.

To extract the mechanical properties that can be used in the FEA indentation simulation to reproduce the experimentally measured load-displacement curves, the following procedure was developed using the optimization module of COMSOL. Starting from an initial guess of E and σ_y, a corresponding load-displacement curve is generated through FEA simulation. The sum of the square of the difference between experimental and FEA simulation results at assigned data point is called the least-square objective. The parameters that minimize the least-square objective were found using BOBYQA method in the optimization module. Finally, these fitted E and H values are shown in Table 1 for A5 and A20. Fig. 4(b) demonstrates good agreement between experiment and simulation by using these fitted parameters. Such mechanical properties are then used in the tribocorrosion simulation in Section 4.

3.2. Extraction of corrosion properties

The corrosion properties of Al alloys were extracted from the experimentally measured polarization curves of A5 and A20, as shown in Fig. 5. Because all potentials were measured versus a Ag/AgCl reference in the experiment, all potential is reported with respect to Ag/AgCl for all following calculation and results. After considering the ion concentration and pH value, the equilibrium potential is -1.98 V vs. Ag/AgCl for the cathodic and -0.25 V vs. Ag/AgCl for the anodic reaction, calculated using Eqs. (1) and (2). First, the anodic and cathodic Tafel slopes are generated by fitting two straight lines tangent to the polarization curve at 100 mV higher and lower than the open circuit potential respectively (Fig. 5). The exchange current densities for anodic and cathodic reactions are then determined based on the procedure described in Fig. 1. The complete set of corrosion parameters are

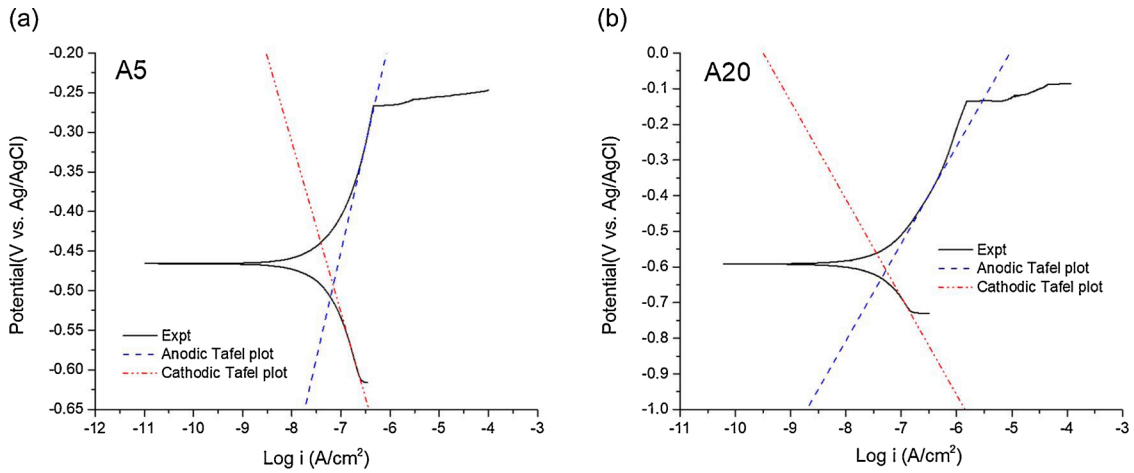

Fig. 5. The experimentally measured potentiodynamic polarization curves and fitted Tafel plots for (a) A5 and (b) A20.

summarized in Table 2 for both alloys.

4. FEA simulation results and validation

4.1. Contact mechanics validation using analytical theory

The FEA model was first validated using analytical Hertzian contact theory [45] by simulating an elastic non-adhesive ball-on-plate contact problem. The ball was assumed to be 4 mm in diameter, with E = 1144.98 GPa and $\nu = 0.3$, indenting on a plate under 10 N load. The plate material was assumed to have E = 108.83 GPa and $\nu = 0.3$. Fig. 6 shows the FEA results of maximum shear stress distribution along the loading direction in the plate material as a function of distance from the surface. It can be seen that the simulated results are in good agreement with those calculated by Hertzian theory, validating the FEA model for an accurate representation of the contact mechanics between two bodies.

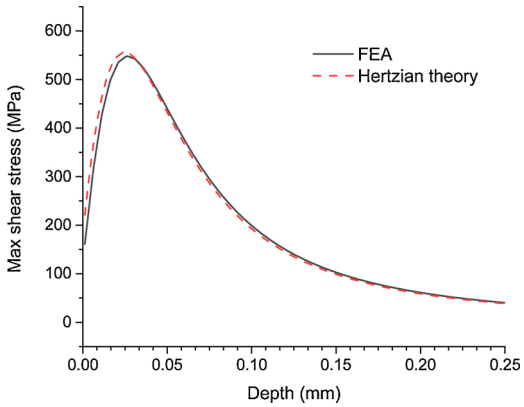

Fig. 6. Maximum subsurface shear stress as a function of distance from the surface of a plate during ball-on-plate indentation calculated from FEM simulation (solid line) and Hertzian contact theory (dashed line).

4.2. FEA simulation results and experimental validation

Next, the FEA model was applied to simulate the pure wear, pure corrosion, and tribocorrosion of A5 and A20, following the procedures detailed in Section 2, using material properties extracted from Section 3. The 3D plot in Fig. 7 shows the von Mises stress and plastic strain distribution inside A5 sample during wear. To make a more straightforward comparison between mechanical state of A5 and A20, the y-z plane at x = 0 was sliced out to demonstrate the 2D plot of stress and strain distribution, as shown in Fig. 8. Fig. 8 (a) and (e) show the von Mises stress (σ_{vM}) distribution inside the sample and indenter at the maximum load, which corresponds to the situation when the counter body slides right onto this cross-sectional area of the sample during wear. Fig. 8 (b, f) and (c, g) show the residual stress σ_{vM} and plastic strain distribution respectively when the indenter has passed the area (note all elastic strains were completely recovered during unloading). The wear tracks were generated by the algorithm as discussed in Section 2.3 using the result of plastic strain are plotted in Fig. 8 (d, h). It could be observed that A5 suffers more severely plastic deformation than A20, with a larger plastic zone size and higher maximum strain of 25 %. The friction coefficient also affects the mechanical response of the sample. In the FEA model, three values of μ (0, 0.3, and 0.6) were studied. As demonstrated in Fig. 9, as μ decreases, the stress and strain decreases, especially for regions close to the surface. For μ = 0.6 and 0.3, the maximum stress and strain is concentrated at the surface. When μ decreases to 0, which resembles the case of a perfectly frictionless surface, the maximum stress and strain both shifts to below the surface, in agreement with Hertzian contact theory. For simplicity, corrosion simulations presented hereafter is carried out assuming μ = 0.

Pure corrosion simulation results of A5 and A20 (after wear and unloading) are shown in Fig. 10. It is noted that the depassivation and wear-corrosion synergy effect is turned off in this step to resemble the case of pure corrosion. The deformed surface geometry, instead of flat surfaces, was used to demonstrate that the synergy effect observed later during tribocorrosion is not caused by the geometry of the wear track. The electrolyte potential (φ_{elec}) distributed uniformly in the solution, as shown in Fig. 10 (a) and (b). Since the open circuit potential φ_{oc} is related to the electrolyte potential as $\varphi_{oc} = -\varphi_{elec}$, the simulated φ_{oc} is

Table 2
Summary of corrosion kinetic parameters for A5 and A20, extracted from potentiodynamic polarization experiments [6,32].

Sample ID	Tafel slope (mV/decade)		E_{eq} (V vs. Ag/AgCl)		I_c (A/cm^2)	I_a (A/cm^2)
	Cathodic	Anodic	Cathodic	Anodic		
A5	−215.39	270.59	−1.98	−0.25	1.65×10^{-7}	2.20×10^{-13}
A20	−274.38	272.38	−1.98	−0.25	3.98×10^{-8}	4.90×10^{-13}

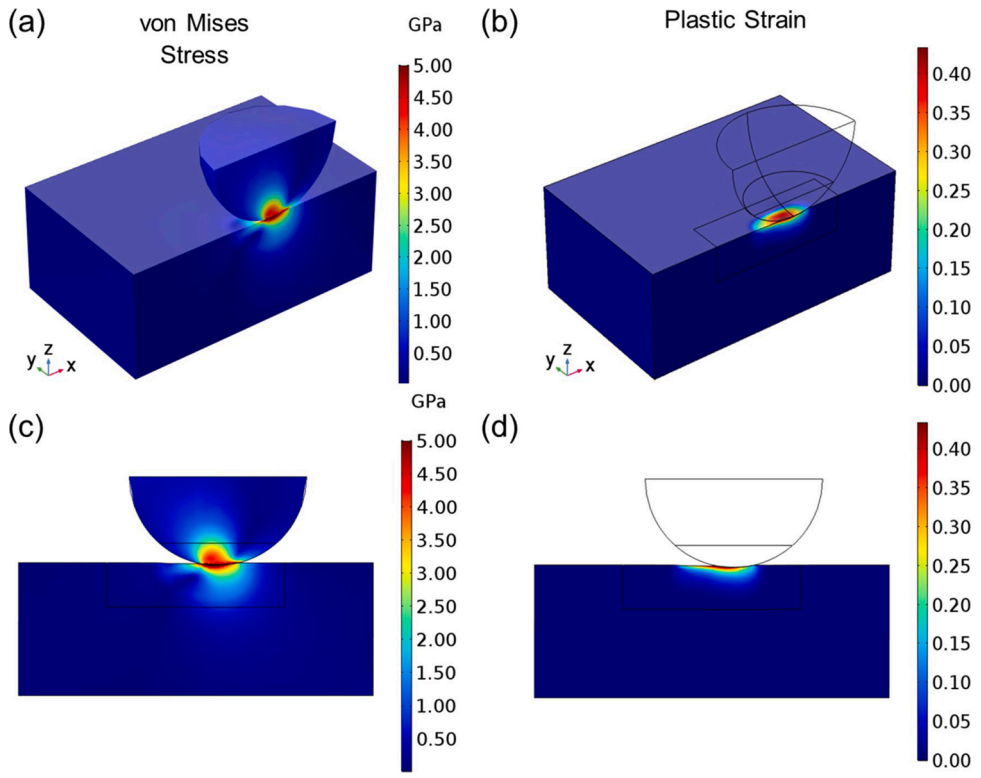

Fig. 7. FEA simulation results of 3D (a) stress and (b) strain distribution in A5 sample under wear, and the corresponding 2D plot of (c) stress and (d) strain in x-z plane.

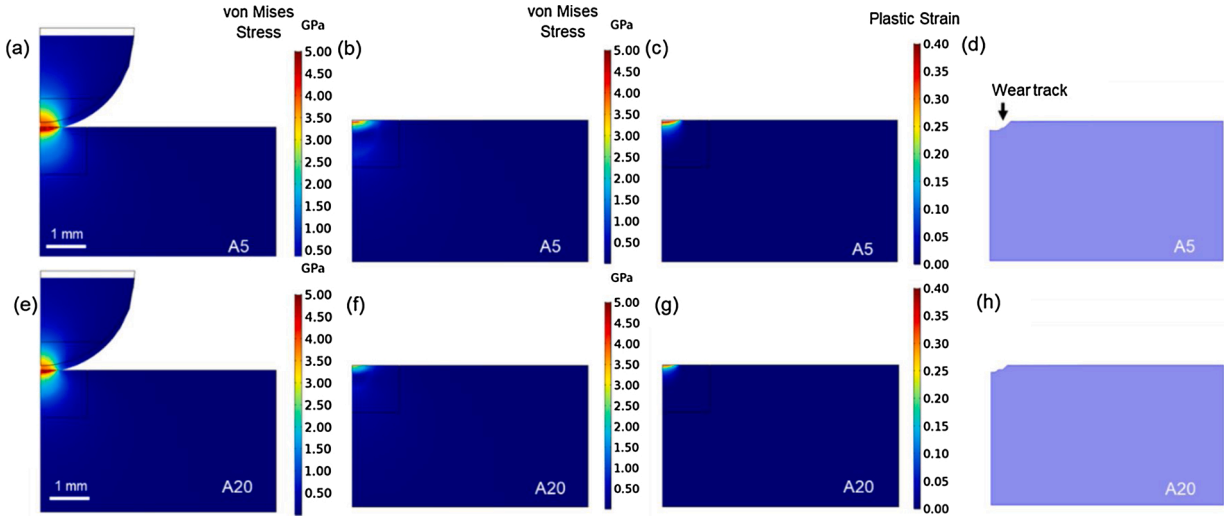

Fig. 8. FEA simulation results of wear tests. (a, e) Subsurface stress during indenter contact, (b, f) subsurface stress, (c, g) plastic strain, and (d,h) the wear track morphology of A5 and A20 after the indenter has passed. All plots are represented from the y-z cross-section (as defined in Fig. 7).

-0.493 V and -0.609 V vs. Ag/AgCl for A5 and A20 respectively. These values are in good agreement with experimentally measured open circuit potential, which is -0.450 V and -0.564 V vs. Ag/AgCl for A5 and A20 respectively. During pure corrosion, material loss takes place uniformly across the surface at a constant rate over time, as shown in Fig. 10 (c) and (d). The simulated corrosion rate is 0.83 and 0.60 μm/year for A5 and A20 respectively, in agreement with their experimentally measured corrosion current trend [32].

The tribocorrosion simulation results are shown in Figs. 11–15, using the same testing parameters as the experiments (i.e. 0.5 N normal load, 5 mm/sec sliding speed, in 0.6 M NaCl aqueous solution [6]). The wear-corrosion synergy was included by accounting the effect of deformation on corrosion, following procedures detailed in Section 2.4. In Fig. 11(a) and (b), the resulting potential distribution inside the electrolyte is plotted along with the strain distribution to demonstrate how the mechanical state of material affects the electrochemical dynamics. It could be seen that the electrolyte potential distribution at the center, where the plastic strain is higher, shifts to a higher value than the rest area for both samples. This leads to a significant increase in electrolyte current density near the deformed area, for example, ~ 0.006 A/m^2 for A5, which means faster material dissolution locally. Within the wear track, the simulated current flow during tribocorrosion

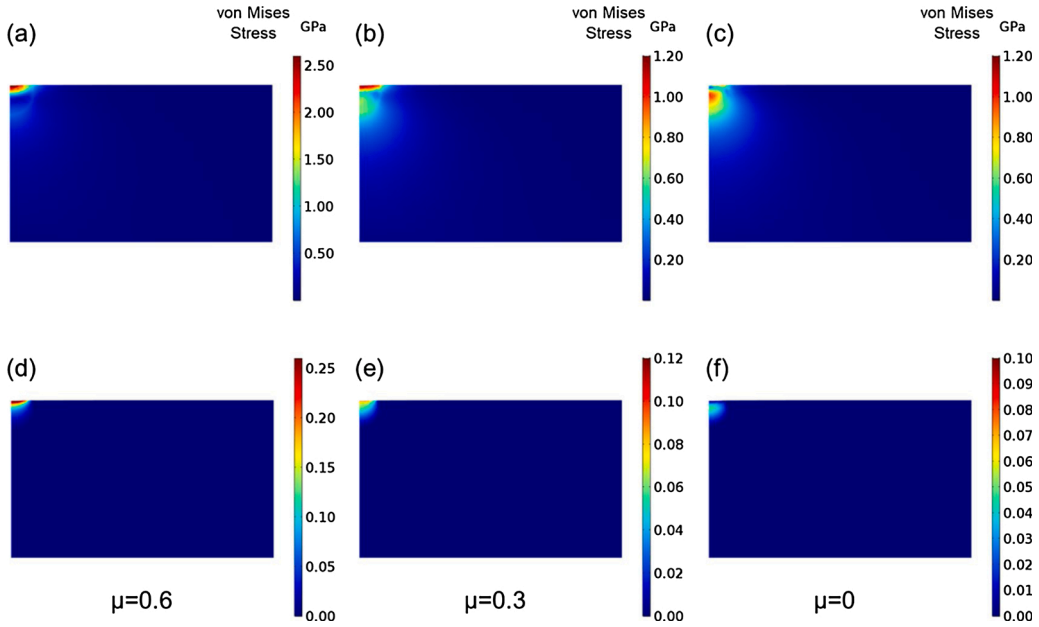

Fig. 9. FEA simulation results of stress and plastic strain left in the A5 sample with different friction coefficient μ: (a, d) μ = 0.6, (b, e) μ = 0.3, (c, f) μ = 0 on the y-z cross-section (as defined in Fig. 7).

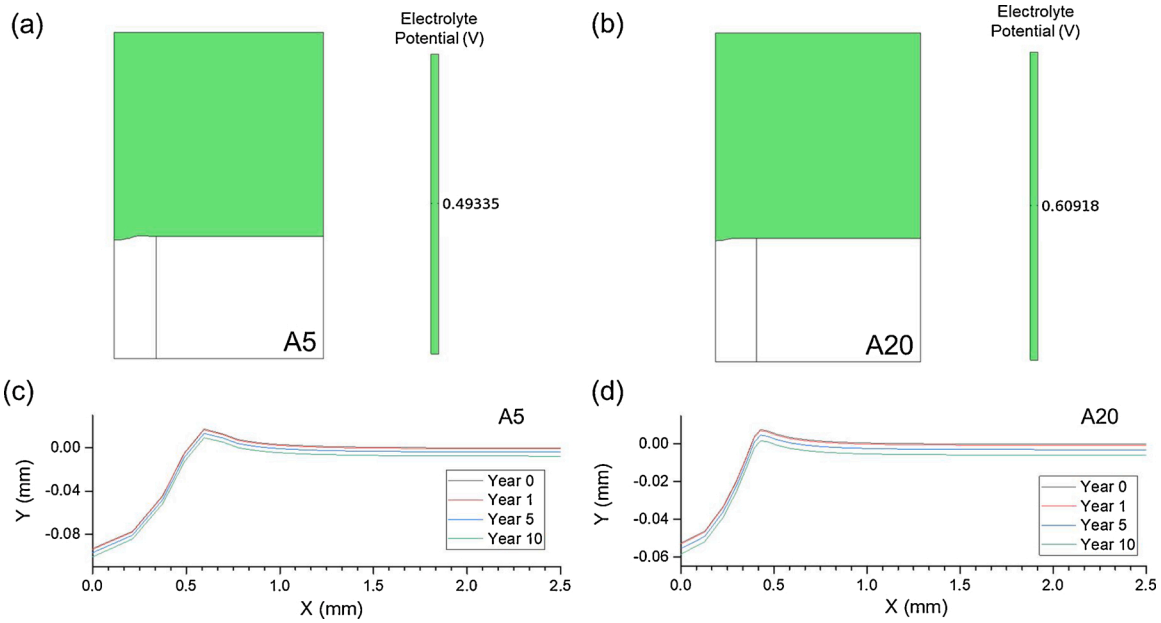

Fig. 10. FEA simulation results of the open circuit potential for (a) A5 and (b) A20 sample, and surface profile evolution as a function of time for (c) A5 and (d) A20 after pure corrosion in 0.6 M NaCl aqueous solution.

is compared to those measured experimentally, as shown in Fig. 12. The sudden increase in current at the beginning of the scratching process due to mechanoelectrical coupling and depassivation, as well as the quasi-periodic fluctuation of corrosion current due to the cyclic depassivation/repassivation process, all agree well with experimental data. The difference in the evolution of surface profile is manifested later in the long-term simulation, as shown in Fig. 13 (a) and (b). Due to the wear-corrosion synergy effect, the indented area corrodes at an obviously faster rate than the rest areas. The corrosion rate drops to a deficient value at places far away from the deformed area (at $r > 0.9$ mm for A5, and at $r > 0.7$ mm for A20). The overall volume loss of both samples is also larger than the pure corrosion circumstance. To decouple the mechanical and chemical wear during tribocorrosion, the total volume loss due to wear (V_{mech}) and corrosion (V_{corr}) is plotted separately in Fig. 13(c), where the volume loss of each sample is calculated using the area integration of the sample domain. It can be seen that the FEA results show the same trend between A5 and A20 as the experiments, with values of the same order of magnitude.

Interestingly, the FEA model also predicts that the mechanochemical synergy is time-dependent. By subtracting the volume loss due to pure corrosion from the volume loss of total corrosion during tribocorrosion, the volume loss caused by wear-corrosion synergy was calculated. The synergy could be further divided into two parts: residual strain induced synergy S_{strain} and depassivation induced synergy $S_{depassivation}$. The former accounts for the accelerated material loss due to the presence of subsurface strain, and the later due to the mechanical removal of the

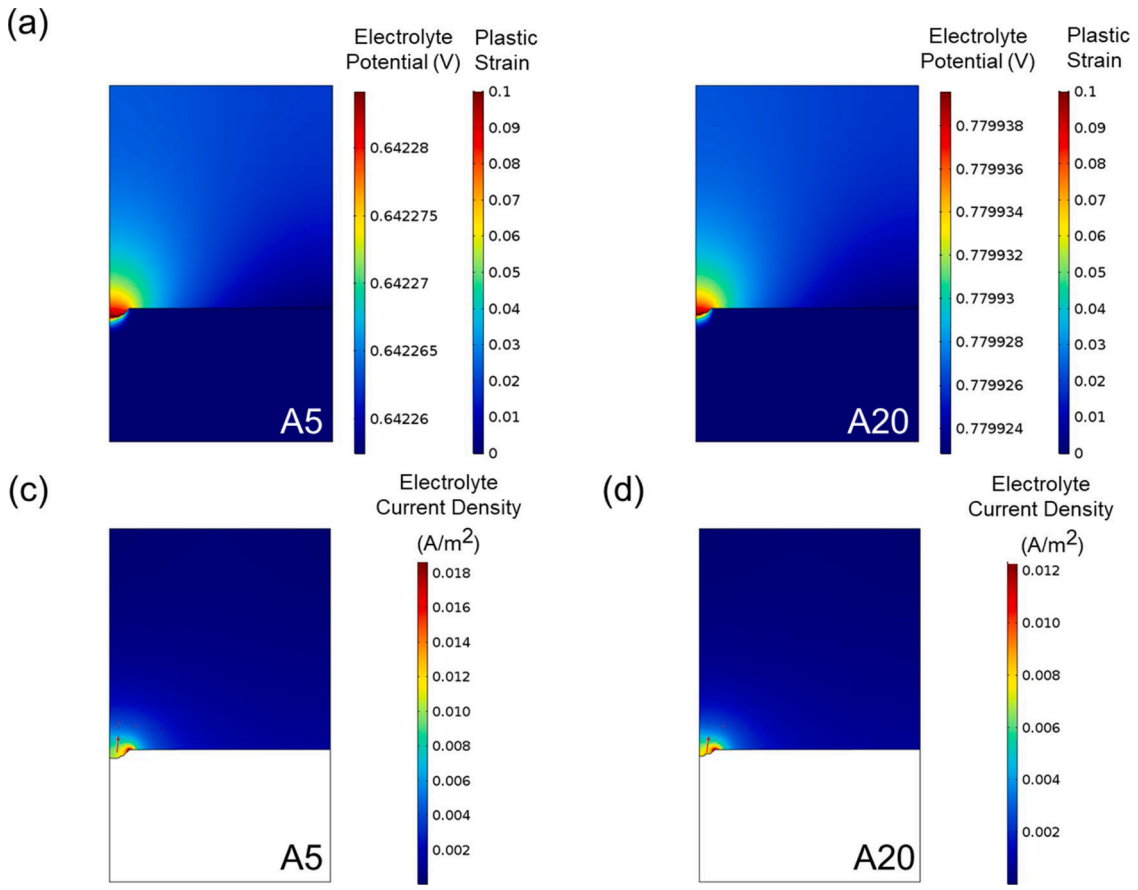

Fig. 11. FEA simulated (a, b) electrolyte potential and subsurface plastic strain distribution, and (c, d) electrolyte current density distribution for A5 and A20 after tribocorrosion under 0.5 N load, 0.5 mm/s sliding speed in 0.6 M NaCl aqueous solution.

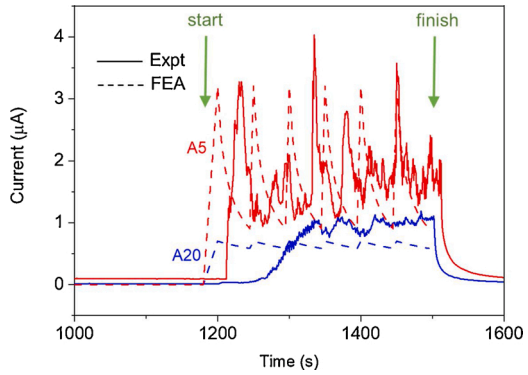

Fig. 12. Comparison of corrosion current change during tribocorrosion of A5 and A20 between experiments (solid lines) and FEA simulation (dashed lines). Arrows indicate the start and finish time of scratching during tribocorrosion.

passive layer. Fig. 14 shows that $S_{depassivation}$ is gradually reduced with time, which is a result of repassivation in the wear track. On the other hand, S_{strain} shows little change as residual strain remains almost unchanged beneath the surface. This also indicates that the sliding frequency could affect the overall synergy. For example, high frequency wear could constantly depassivate the wear track and keep $S_{depassivation}$ at a high value. The depassivation induced synergy would sharply increase at the instance when wear takes place but only have a short-term effect after the scratching stops. In a larger timescale, S_{strain} would sustain its acceleration effect on corrosion in a long period of time even after the scratching stops. This implies that the repassivation ability has more mechanochemical coupling effect during or shortly after scratching, while the mechanical properties have a long-term coupling effect until the deformed layer is completely dissolved.

It is worth noting that the current model only takes apparent contact area in macroscale into account for simulating depassivation. Experimental investigation by Gilbert et al. has indicated that the depassivation for tribocorrosion is actually related to surface morphology at asperity scale [46]. For example, a model developed by Ghanbarzadeh et al. [47] successfully address the influence of surface roughness on wear-corrosion synergy by modeling the real contact area for depassivation based on the boundary element method. Due to the complex kinetics of asperity generation and evolution of different alloy systems, more work is needed in the future to implement and validate the current model to evaluate the effect of nano-scale asperity contact on the tribocorrosion kinetics.

4.3. Prediction of tribocorrosion map

To further explore a generalized relationship between the material properties and wear/corrosion resistance of metals, a parameter sweep was carried out and the tribocorrosion rate (unit: mm^2), defined as the total material loss (unit: mm^3) divided by the sliding distance (unit:mm), is plotted as contour maps against these parameters, as shown in Fig. 15. To evaluate the effects of mechanical properties on the material loss due to mechanical deformation and chemical dissolution, the Young's modulus was swept from 55 MPa to 95 MPa with 6 MPa step size, the yield strength from 1.0 MPa to 5.0 MPa with 0.5 step size, while the corrosion parameters were taken from A5 sample and kept constant. As shown in Fig. 15 (a), materials with lower Young's modulus and higher yield strength are more wear-resistant, which is as expected. Interestingly, it's worth noting that even with the same corrosion properties, the

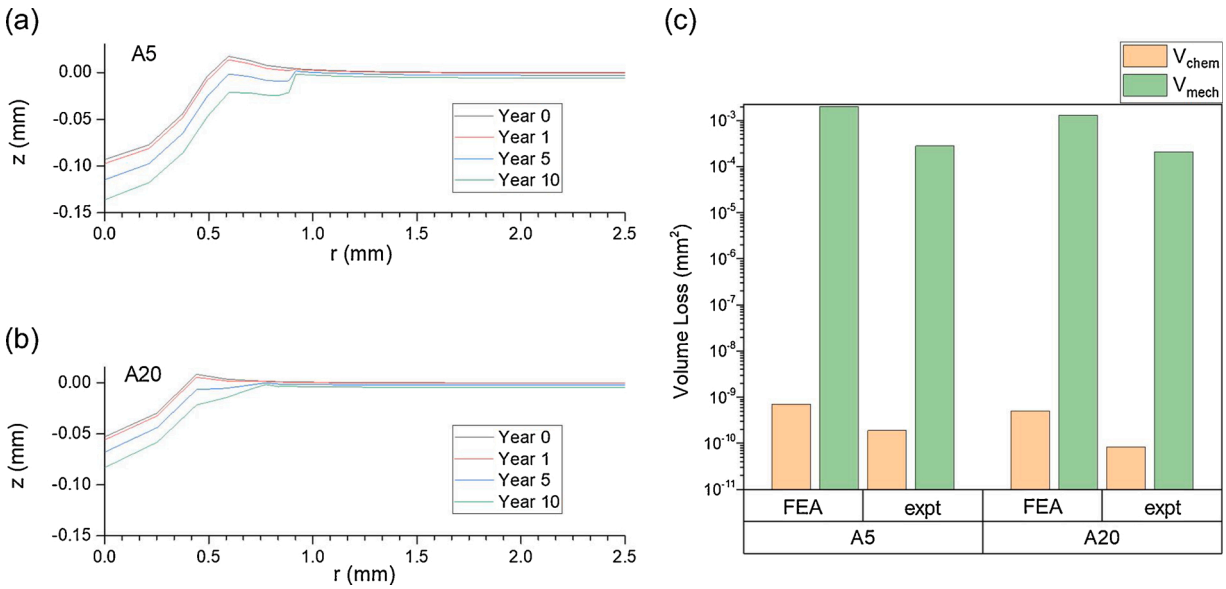

Fig. 13. FEA simulated surface profile change during tribocorrosion for (a) A5 and (b) A20, and (c) comparison between FEA simulated and experimentally measured mechanical and chemical wear for A5 and A20.

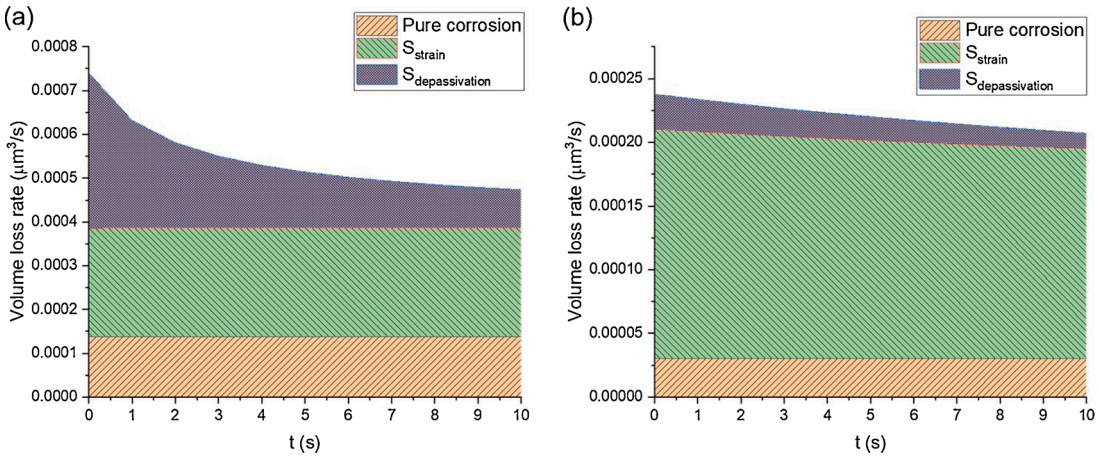

Fig. 14. Volume loss rate from pure corrosion, strain induced synergy and depassivation induced synergy for (a) A5 and (b) A20 with respect to time.

corrosion rate shows a significant difference after deformation. The materials with more optimal mechanical properties would suffer less corrosion, since there will be fewer surface defects caused by plastic deformation.

Fig. 15 (c, d) shows the effects of corrosion parameters on the tribocorrosion behavior, where the cathodic Tafel slope was varied from -280 to −210 mV/decade, the cathodic exchange current density from 2.0×10^{-8} to 2.0×10^{-7} A/cm^2, the anode Tafel slope from 250 to 290 mV/decade, and the anodic exchange current density from 1.0×10^{-13} to 5.0×10^{-13} A/cm^2. Fig. 15 (c) shows that the V_{corr} is insensitive to the cathodic Tafel slope but increases with increasing cathodic exchange current. Fig. 15 (d) shows V_{corr} increases with increasing anodic exchange current density and reducing anodic Tafel slope. Summarizing results in Fig. 15 indicate that materials with low anodic and cathodic exchange current density, low anodic Tafel slope, high yield strength, and low Young's modulus are highly tribocorrosion resistant, thus providing a design guideline for future metals and coatings to be used under extreme conditions.

5. Uncertainty quantification (UQ) study

Sections 3 and 4 introduced the detailed setup of the FEA model and simulation results given different input parameters. Apart from the specific simulation result, the confidence interval of each simulation result is especially important in the system with uncertainties in input parameters and parametric variability. However, because of the computational cost of the FEA model, it is computationally expensive and time-consuming to apply the Monte Carlo simulations method [33] directly for uncertainty quantification. In this work, Gaussian Process (GP) [34] and Neural Network (NN) with dropout [35], two data-driven surrogates, were selected to approximate the FEA model and realize efficient uncertainty quantification [36,37].

The simulation results from the FEA model were preprocessed and split into training and testing data. In data preprocessing, each variable, including six input variables (i.e. Young's modulus, yield strength, anodic and cathodic Tafel slopes, anodic and cathodic exchange current densities) and one output (tribocorrosion rate) variable, was normalized into $[0, 1]$ by using the max-min normalization method. Since each variable has different physical meanings and scales, normalization was necessary to reduce the possibility that the output of the data-driven

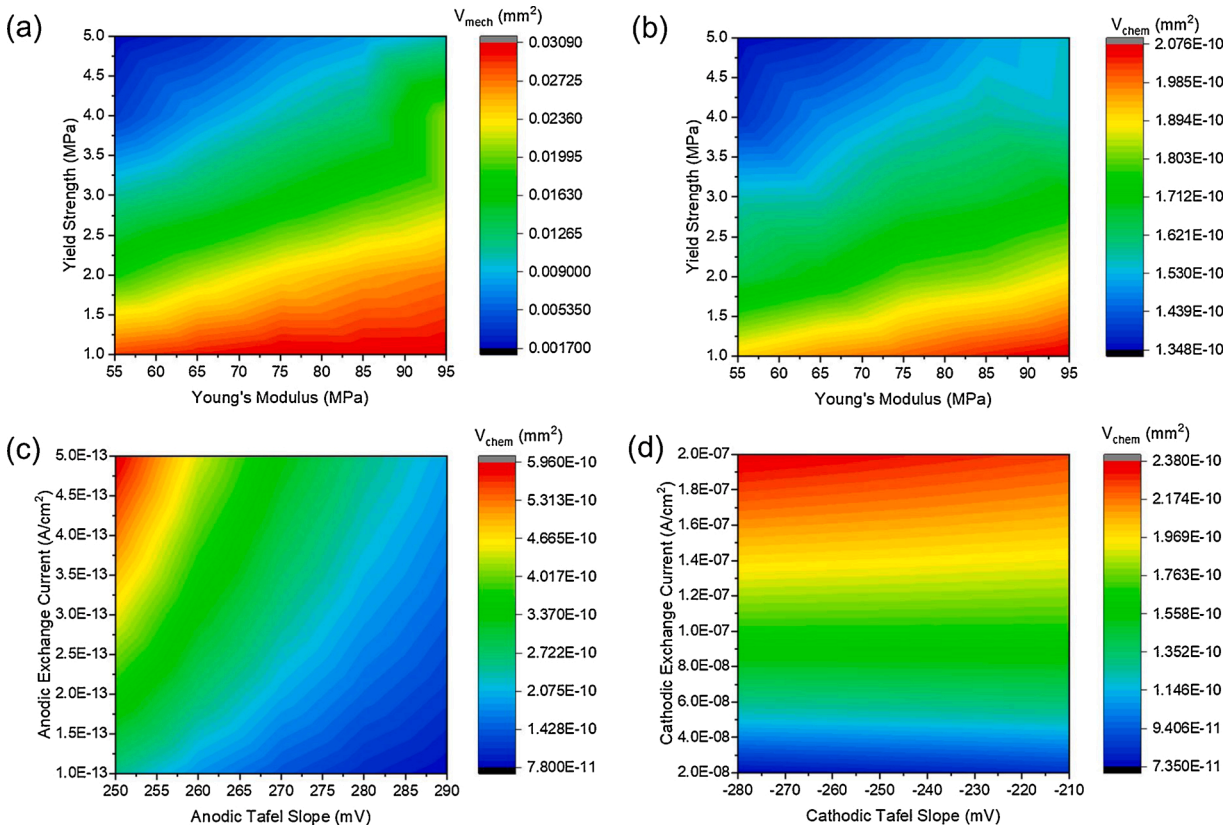

Fig. 15. FEA predicated volume loss rate due to (a) wear and (b) corrosion for materials with different Young's modulus and yield strength, and corrosion rate for materials with different (c) anodic and (d) cathodic reaction properties.

model be dominated by extremely large or small values in these variables. After normalization, 89 simulations were selected as training data to build the surrogates and 17 simulations were selected as testing data to evaluate the surrogates.

In the GP model, instead of finding a deterministic function, it derives the probability distribution over all possible functions that fit the data [34]. The distribution over functions enables the GP to not only generate the predicted value but also generate a confidence interval (CI) associated with each prediction. Similarly, NN with dropout can also be regarded as a distribution over all possible functions [35], which enables the model to estimate the expectation and variance of the predictive distribution empirically. The advantages of these two surrogates include (i) they are proved to be powerful methods in modeling non-linear functions; (ii) both of them are efficient to reduce the computational cost of the original FEA simulations; (iii) as data-driven surrogates, they can learn model parameters from historical data to estimate the average and variance of output value for new samples (i.e. new FEA simulations).

After building the surrogates on the training data, the surrogates were evaluated on the testing data. Firstly, the accuracy of surrogates was evaluated. Only surrogate model with high accuracy could precisely approximate the FEA model and replace FEA in UQ analysis. Because the scale of the output is around 10^{-10}, the mean absolute percentage error (MAPE) was selected as the evaluation metric to avoid the impacts of ultra-small scale. There might be slight differences between the outputs from the surrogate model and FEA, but as long as the differences are within a certain confidence interval (CI), i.e. 95 % CI, the UQ analysis

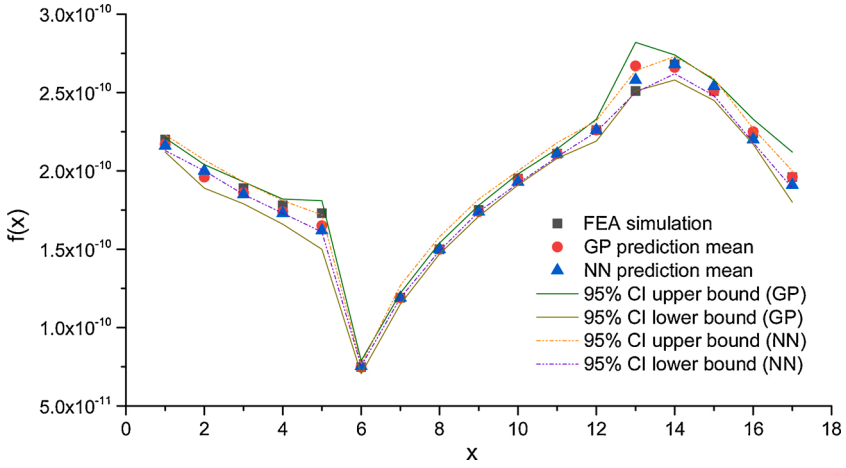

Fig. 16. Visualization of UQ analysis where the vertical axis $f(x)$ represents the output values and the horizontal axis x represents the index of observations.

given by the surrogates are meaningful to our FEA. The results of surrogates show that the MAPE of GP is 1.1 %, while the MAPE of NN with dropout is 1.5 %. GP is marginally better than NN with dropout. The confidence intervals of these two models are plotted in Fig. 16, where the vertical axis $f(x)$ represents the output values and the horizontal axis x represents the index of observations (17 in total). These results show that most of predictions given by GP and NN were quite close to observations, which means that the surrogates are accurate enough to replace FEA in UQ analysis. Specifically, only one observation from FEA was found outside the 95 % CI according to NN with dropout, while all the FEA results in Section 4 were located within 95 % CI according to the GP surrogate. Based on these results, several additional conclusions can be drawn: (1) UQ analysis and the corresponding confidence interval could be used to augment each simulation result given by FEA; (2) GP is more accurate than NN with dropout for UQ of tribocorrosion datasets; (3) the learned GP model can be used to approximate the UQ in FEA and calculate CI for new simulation inputs.

6. Conclusions

A multiphysics FEA model was successfully built for metal tribocorrosion and validated using experimental results of Al alloys. A procedure for material property extraction from experiments was developed to extract Young's modulus, yield strength, exchange current density, and Tafel slopes to be used as model inputs. Using the developed FEA model, the effects of material properties on the degradation mechanism during tribocorrosion was studied. The results showed accelerated corrosion at areas near the wear track that suffered from severe deformation, as well as a time-dependent behavior of the wear-corrosion synergy due to non-uniform subsurface residual stress. The model helped not only in understanding the mechanism of tribocorrosion, but also predicted material loss under different mechanical and electrochemical properties, providing a guideline for future material design and optimization against tribocorrosion. Finally, the FEA results were successfully augmented with a confidence interval by implementing uncertainty quantification using data-driven surrogates. Gaussian Process was chosen over Neural Network due to its better correspondence with the FEA result. In this way, the FEA model not only generate specific simulation results but also the confidence interval for each simulation, which takes the uncertainties and variabilities in input parameters into consideration.

CRediT authorship contribution statement

Kaiwen Wang: Investigation, Validation, Writing - original draft. **Yinan Wang:** Methodology, Software, Writing - original draft. **Xiaowei Yue:** Supervision, Writing - review & editing. **Wenjun Cai:** Conceptualization, Supervision, Writing - review & editing.

Declaration of Competing Interest

The authors report no declarations of interest.

Acknowledgements

This research was financially supported by the US National Science FoundationDMR-1856196 and CMMI-1855651.

References

[1] K. Pondicherry, D. Fauconnier, P. De Baets, Synergism in multi-asperity abrasion-corrosion of martensitic and dual phase steels in three aqueous electrolytes, Wear 452 (2020).
[2] S. Roy, et al., Flow-induced failure mechanisms of copper pipe in potable water systems, Corros. Rev. 36 (5) (2018) 449–481.
[3] Y.S. Kim, et al., Influence of a simulated deep sea condition on the cathodic protection and electric field of an underwater vehicle, Ocean. Eng. 148 (2018) 223–233.
[4] M. Buciumeanu, et al., Tribocorrosion behavior of hot pressed CoCrMo alloys in artificial saliva, Tribol. Int. 97 (2016) 423–430.
[5] H. Mraied, W.B. Wang, W.J. Cai, Influence of chemical heterogeneity and microstructure on the corrosion resistance of biodegradable WE43 magnesium alloys, J. Mater. Chem. B 7 (41) (2019) 6399–6411.
[6] H. Mraied, W.J. Cai, The effects of Mn concentration on the tribocorrosion resistance of Al-Mn alloys, Wear 380-381 (2017) 191–202.
[7] C. Vargel, Corrosion of Aluminium, 1st ed., Elsevier, Amsterdam; Boston, 2004 xxxii, 626 p.
[8] Z. Szklarska-Smialowska, Pitting corrosion of aluminum, Corros. Sci. 41 (9) (1999) 1743–1767.
[9] M.O. Speidel, Stress-corrosion cracking of aluminum-alloys, Metall. Trans. A 6 (4) (1975) 631–651.
[10] C.C. Streinz, et al., Analysis of passive film growth by dynamic imaging microellipsometry, J. Electrochem. Soc. 139 (3) (1992) 711–715.
[11] P. Jemmely, S. Mischler, D. Landolt, Tribocorrosion behaviour of Fe-17Cr stainless steel in acid and alkaline solutions, Tribol. Int. 32 (6) (1999) 295–303.
[12] S. Mischler, S. Debaud, D. Landolt, Wear-accelerated corrosion of passive metals in tribocorrosion systems, J. Electrochem. Soc. 145 (3) (1998) 750–758.
[13] S. Mischler, A. Spiegel, D. Landolt, The role of passive oxide films on the degradation of steel in tribocorrosion systems, Wear 225 (1999) 1078–1087.
[14] A.C. Vieira, et al., Mechanical and electrochemical deterioration mechanisms in the tribocorrosion of Al alloys in NaCl and in NaNO3 solutions, Corros. Sci. 54 (2012) 26–35.
[15] J.O. Bello, R.J.K. Wood, J.A. Wharton, Synergistic effects of micro-abrasion–corrosion of UNS S30403, S31603 and S32760 stainless steels, Wear 263 (1–6) (2007) 149–159.
[16] M.R. Thakare, et al., Exposure effects of strong alkaline conditions on the microscale abrasion–corrosion of D-gun sprayed WC–10Co–4Cr coating, Tribol. Int. 41 (7) (2008) 629–639.
[17] A. Chatterjee, et al., Nanoscratch study of hard HfB2 thin films using experimental and finite element techniques, Wear 268 (5-6) (2010) 677–685.
[18] Y.J. Park, G.M. Pharr, Nanoindentation with spherical indenters: finite element studies of deformation in the elastic-plastic transition regime, Thin Solid Films 447 (2004) 246–250.
[19] C. Walter, et al., Finite element simulation of the effect of surface roughness on nanoindentation of thin films with spherical indenters, Surf. Coat. Technol. 202 (4-7) (2007) 1103–1107.
[20] J.X. Zhao, F. Sadeghi, H.M. Nixon, A finite element analysis of surface pocket effects in Hertzian line contact, Journal of Tribology-Transactions of the Asme 122 (1) (2000) 47–54.
[21] S.R. Cross, S. Gollapudi, C.A. Schuh, Validated numerical modeling of galvanic corrosion of zinc and aluminum coatings, Corros. Sci. 88 (2014) 226–233.
[22] Y.C. Wang, et al., Numerical simulation of micro-galvanic corrosion in Al alloys: steric hindrance effect of corrosion product, J. Electrochem. Soc. 164 (14) (2017) C1035–C1043.
[23] L.T. Yin, et al., Numerical simulation of micro-galvanic corrosion of Al alloys: effect of chemical factors, J. Electrochem. Soc. 164 (13) (2017) C768–C778.
[24] L.T. Yin, et al., Numerical simulation of micro-galvanic corrosion of Al alloys: effect of density of Al(OH)(3) precipitate, Electrochim. Acta 324 (2019).
[25] L.Y. Xu, F. Cheng, A finite element based model for prediction of corrosion defect growth on pipelines, Int. J. Press. Vessel. Pip. 153 (2017) 70–79.
[26] L.Y. Xu, Y.F. Cheng, Development of a finite element model for simulation and prediction of mechanoelectrochemical effect of pipeline corrosion, Corros. Sci. 73 (2013) 150–160.
[27] H.T. Wang, E.H. Han, Simulation of metastable corrosion pit development under mechanical stress, Electrochim. Acta 90 (2013) 128–134.
[28] J. Chen, W.J. Cai, Effect of scratching frequency on the tribocorrosion resistance of Al-Mn amorphous thin films, Wear 426 (2019) 1457–1465.
[29] S.C. Ferreira, et al., Microstructural characterization and tribocorrosion behaviour of Al/Al3Ti and Al/Al3Zr FGMs, Wear 270 (11–12) (2011) 806–814.
[30] G.S. Frankel, Pitting corrosion of metals. A review of the critical factors (vol 145, pg 2186, 1998), J. Electrochem. Soc. 145 (8) (1998), 2970-2970.
[31] D. Jones, Principles and Prevention of Corrosion, Prenti~e-Hall, Inc., 1996.
[32] H. Mraied, W.J. Cai, A.A. Sagues, Corrosion resistance of Al and Al-Mn thin films, Thin Solid Films 615 (2016) 391–401.
[33] R.Y. Rubinstein, D.P. Kroese, Simulation and the Monte Carlo Method, third edition, 2016, pp. 1–414.
[34] D. Crevillen-Garcia, et al., Gaussian process modelling for uncertainty quantification in convectively-enhanced dissolution processes in porous media, Adv. Water Resour. 99 (2017) 1–14.
[35] Y. Gal, Z. Ghahramani, Dropout as a bayesian approximation: representing model uncertainty in deep learning, International Conference on Machine Learning (2016).
[36] G.G. Wang, S. Shan, Review of metamodeling techniques in support of engineering design optimization, J. Mech. Des. 129 (4) (2007) 370–380.
[37] S. Razavi, B.A. Tolson, D.H. Burn, Review of surrogate modeling in water resources, Water Resour. Res. 48 (2012).
[38] W.C. Oliver, G.M. Pharr, Measurement of hardness and elastic modulus by instrumented indentation: advances in understanding and refinements to methodology, J. Mater. Res. 19 (1) (2004) 3–20.

[39] N.A. Sakharova, et al., Comparison between Berkovich, Vickers and conical indentation tests: a three-dimensional numerical simulation study, Int. J. Solids Struct. 46 (5) (2009) 1095–1104.
[40] D. Nelias, V. Boucly, M. Brunet, Elastic-plastic contact between rough surfaces: proposal for a wear or running-in model, J. Tribol.-Trans. ASME 128 (2) (2006) 236–244.
[41] R. Bosman, D.J. Schipper, Transition from mild to severe wear including running in effects, Wear 270 (7-8) (2011) 472–478.
[42] Y.S. Tak, K.R. Hebert, Initial events during the passivation of rapidly dissolving aluminum surfaces, J. Electrochem. Soc. 141 (6) (1994) 1453–1459.
[43] E.m.M. Gutman, Mechanochemistry of Solid Surfaces, World Scientific, Singapore; River Edge, NJ, 1994 ix, 322 p.
[44] M. Hordon, B.J.A.M. Averbach, X-ray measurements of dislocation density in deformed copper and aluminum single crystals, Acta Metall. 9 (3) (1961) 237–246.
[45] A.C. Fischer-Cripps, The hertzian contact surface, J. Mater. Sci. 34 (1) (1999) 129–137.
[46] S.M. Smith, J.L. Gilbert, Compliant interfaces and fretting corrosion of modular taper junctions in total hip implants: the micromechanics of contact, Tribol. Int. 151 (2020).
[47] A. Ghanbarzadeh, et al., A new asperity-scale mechanistic model of tribocorrosive wear: synergistic effects of mechanical wear and corrosion, J. Tribol. 141 (2) (2019).